Journal of Manufacturing Processes 83 (2022) 300–312

Contents lists available at ScienceDirect

Journal of Manufacturing Processes

journal homepage: www.elsevier.com/locate/manpro

A three-dimensional wire-feeding model for heat and metal transfer, fluid flow, and bead shape in wire plasma arc additive manufacturing

Xin Chen *, Chong Wang *, Jialuo Ding, Phillippe Bridgeman, Stewart Williams

Welding and Additive Manufacturing Centre, Cranfield University, Cranfield MK43 0AL, UK

ARTICLE INFO

Keywords:
WAAM
Wire-feeding
Metal transfer
Flow pattern
Bead shape

ABSTRACT

A three-dimensional wire-feeding model has been developed to study the transient coupling behaviour of heat and metal transfer, fluid flow, and solidified bead shape in wire plasma arc additive manufacturing (WPAAM). A novel surface heat source model considering the arc energy shading effect is proposed and adopted. An improved momentum source of the arc force considering the arc pressure shading effect is also developed and used. This model has been used to study the metal transfer dynamics, flow patterns, and bead shape of the WPAAM process with a wire-feeding speed (WFS) of 1–5 m/min. The simulated results agreed reasonably with the experimental data. As the WFS increased from 1 to 5 m/min, three different metal transfer modes were observed, which changed from globular droplet mode to droplet-liquid bridge mode and solid-liquid bridge mode. Detailed metal transfer information was analysed, including metal transfer position, shape, average temperature, and main driving force. The effects of the arc shading and metal transfer on the melt pool dynamics and bead shape were simulated and discussed. A periodic flow pattern of the melt pool produced by the metal transfer impact causes ripples or even humping defects. As the WFS increased, the melt pool depression gradually disappeared due to the arc pressure shading effect. When the WFS increased to 5 m/min, a temperature drop of about 140 K in the central melt pool, caused by the arc energy shading effect and cold metal transfer, weakened the lateral flow significantly, which explained the decrease of bead width at a large WFS. The results demonstrate that the developed wire-feeding model and findings could be used as a theoretical tool and basis to better understand the underlying physical mechanisms and achieve bead shape control in the WAAM process.

1. Introduction

Wire arc additive manufacturing (WAAM) is an advanced processing technology which is well known for its advantages of high deposition rate, high energy efficiency and low equipment cost [1–5]. It attracts more and more attention in recent years since it shows great potential to manufacture medium or large-scale metal parts in aerospace, transport, and marine sectors [6–8]. Wire plasma arc additive manufacturing (WPAAM) is one type of WAAM, which utilises a high-density plasma arc as the heat source [9,10]. It is suitable technology to achieve very-high deposition rate, low surface roughness, high material performance, and near-net-shape structures [10].

In the WPAAM process, the filler wire is heated and melted by the plasma arc and then transferred into the melt pool on the substrate or previous layers. The fluid in the melt pool flows sideways and backwards and then solidifies as the plasma arc moves forward. The controllable bead shape geometry has been tried to achieve since a very early demonstrated stage of the WAAM process [11–13]. It is also one of the most critical factors of the quality of the WPAAM components. However, the mechanism of bead shape formation, which is determined by the coupling behaviour of heat and mass transfer and fluid flow, is not well understood. Experimental investigation plays a crucial role in understanding and optimising the process. Based on sound experience and many trial and error experiments, it is usually possible to find and adopt an improved process parameter window. However, it can be time-consuming and expensive. Additionally, it is still challenging for experiments to understand the effects of complex melted flow behaviour.

Comprehensive phenomenological models can be used as a beneficial tool to understand the fundamental heat and mass transfer and fluid flow process. Computational fluid dynamics (CFD) modelling work [14–23] of arc welding has accumulated rich experience and knowledge about the complex physical behaviours of arc, droplet, melt pool and bead shape, and are good references to model the WAAM process. In addition, in wire-based additive manufacturing (AM) processes, the

* Corresponding authors.
E-mail addresses: x.chen1@cranfield.ac.uk (X. Chen), chong.wang1@cranfield.ac.uk (C. Wang).

https://doi.org/10.1016/j.jmapro.2022.09.012
Received 10 September 2021; Received in revised form 27 August 2022; Accepted 8 September 2022
Available online 19 September 2022

metal transfer significantly influences the process stability and fluid flow behaviours [10,24,25]. In wire-based electron beam AM process, Hu et al. [25] numerically showed how the metal transfer mode influenced the melt pool flow and stability and clarified the mechanism, although the process is much different from the WPAAM process in this study. In their modelling results, the energy shaded by the filler wire can be seen. In the WPAAM process, recent experimental work of Chong et al. [10] showed that the arc pressure-induced keyhole defects were suppressed by using a thick filler wire due to the arc shading by the wire. These demonstrate that the filler wire and metal transfer process can significantly affect the heat transfer and fluid flow behaviours and should be considered in a comprehensive modelling work.

In recent years, numerous CFD models [26–31] of WAAM processes have been developed, but few of them considered the wire-feeding process, which includes the wire feeding, melting and metal transfer behaviours. Ou et al. [26] developed a 3D heat transfer and fluid flow model of WAAM and utilised it to investigate the thermal and velocity fields, deposit shape and size, cooling rates and solidification parameters. They found that convection dominates the heat transfer inside the melt pool. The developed model has also been used to help form ideal deposit shape and size in the circle route and triangle route in the WAAM process [27]. However, their model has not considered the wire-feeding process but simplifies the metal transfer as a source term. So, their modelling failed to show the important effects of the wire-feeding process on the thermal distribution and fluid flow dynamics in the melt pool. Hejripour et al. [28] proposed a heat transfer and fluid flow model to simulate a dissimilar substrate gas tungsten arc welding-based (GTAW-based) WAAM process. Their modelling reasonably predicted the element distributions and deposited bead shape. Ogino et al. [29] developed a three-dimensional (3D) model to investigate the multilayer Metal Active Gas (MAG)-based WAAM process. Their model was used to investigate the influence of cooling temperature and welding direction between passes. Bai et al. [30] developed a 3D model to investigate the heat transfer and fluid flow in the multilayer WPAAM process. They simulated the thermal fluid behaviour of the 1st, 2nd, and 21st layer depositions and demonstrated that the Marangoni force plays a crucial role in the melt pool fluid flow. However, similar to the model of Ou et al. [26], the three models mentioned above also simply treated the metal transfer as a source term. In the practical WAAM process, the wire melting and melt transfer information, such as the shape, temperature, velocity, and position is significantly different and challenging to be captured by experiments. Zhou et al. [31] developed a 3D model of arc based on magnetic fluid dynamics to simulate the arc-based additive forming process. This model weakly coupled the arc, droplet and melt pool dynamics, and the calculated melt pool morphology and cross-section profile were consistent with the experimental data. However, their model still did not incorporate the wire-feeding process and failed to accurately calculate the metal transfer effect on the melt pool dynamics. Therefore, those models [26–31] may be difficult to be used to gain insight into the complex fluid flows and bead formation in the WPAAM process.

Recently, a multiphysics model developed by Cadiou et al. [32,33] considered a one-dimensional (vertical direction) wire-feeding process in the cold metal transfer (CMT) AM process. The results showed the significant role played by the metal transfer effect which strongly influenced the melt pool size, the fluid flow and the temperature field. In the WPAAM process, the plasma arc from a tungsten electrode melts an inclined feeding wire so that there is likely a shading effect from the wire, which is different from the CMT process.

This paper reports the development of a 3D wire-feeding model for the transient coupling behaviour of heat and metal transfer, fluid flow, and solidified bead shape in the WPAAM process. In the model, the wire-feeding process is incorporated by employing the mixture theory and Euler method. The arc energy shading effect and arc pressure shading effect have been considered by proposing a novel arc surface heat source model and an improved momentum source of the arc force. The transient evolution of metal transfer dynamics and flow patterns and the final bead shape at the WFS of 3 m/min are reproduced and investigated. The typical modes and information about metal transfer with the different WFS of 1–5 m/min are further investigated. The fluid flow behaviour coupled with the metal transfer dynamics is simulated, and the significant effects of the arc shading and metal transfer on the melt pool dynamics and bead formation are discussed. The simulated metal transfer is compared with the videos captured by a process camera, the predicted flow patterns are compared to the solidified ripples on the bead surface and literature data, and the bead shape is compared with the metallographic image.

2. Materials and methods

2.1. Experiments

The WPAAM experiment was conducted in a glove chamber filled with pure argon gas, as shown in Fig. 1. A DC EWM T552 Tetrix Plasma power source was used. The plasma gas flowrate and shield gas flowrate were 0.8 l/min and 8 l/min, respectively. The nozzle diameter was 3.9 mm, and the vertex angle of the tungsten electrode was 45°. The wire feeder was fixed with the moving torch with an angle of 25° to the horizontal plane. The materials of both the filler wire and the substrate were all Ti6Al4V alloys. Their chemical compositions are shown in Table 1. The diameter of the wire was 1.2 mm, and the substrate dimensions were 300 mm, 200 mm, and 7 mm in the travel speed, transverse and thickness directions, respectively.

A single layer deposition which is the fundamental feature of WPAAM, was conducted in the experiments and the simulations to investigate the metal transfer dynamics and bead shape formation with different WFS. A welding process camera (Xiris XVC-1000e) was applied to capture and record the process with a frame rate of 25 Hz during the deposition process. After deposition, the bead cross-sections were measured by metallographic analysis and microscopic inspection. Table 2 lists the deposition parameters used in the experimental work and the simulations.

2.2. Modelling

In the novel 3D wire-feeding model, the wire movement was described by using the mixture theory and Euler method [25]. To make the computation tractable, the geometry was set to be limited in the region around the melt pool, which is shown in Fig. 2. During the simulation, it was assumed that the substrate (rather than the wire feeder and plasma torch) was moving. The liquid Metal was considered to be a laminar, Newtonian, incompressible fluid. The symbols used in the modelling are listed in Table 3.

2.2.1. Governing equations

In the whole domain, for an incompressible fluid multiphase flow, the governing equations of mass, momentum, and energy conservation are the following:

$$\nabla \bullet \mathbf{u} = 0 \tag{1}$$

$$\rho\left(\frac{\partial \mathbf{u}}{\partial t} + \left((\mathbf{u}-\mathbf{u}_t)\bullet\nabla\right)\mathbf{u}\right) = -\nabla p + \nabla\bullet(\mu\nabla\mathbf{u}) + \mathbf{F}_{\mathrm{v}} + \mathbf{F}_{\mathrm{s}} + \mathbf{F}_{\mathrm{m}} \tag{2}$$

$$\rho\left(\frac{\partial h}{\partial t} + \left((\mathbf{u}-\mathbf{u}_t)\bullet\nabla\right)h\right) = \nabla\bullet(k\nabla T) + q_{heat} + q_{loss} \tag{3}$$

2.2.2. Phase transformation interfaces

In this model, the liquid-gas interface is free to deform during the WPAAM process. Here, we used the volume of fluid (VOF) method [34] to track dynamic free surfaces. In the VOF method, the volume fraction α represents the phases: $\alpha = 0$ means the cells are full of metal fluid; $\alpha = 1$

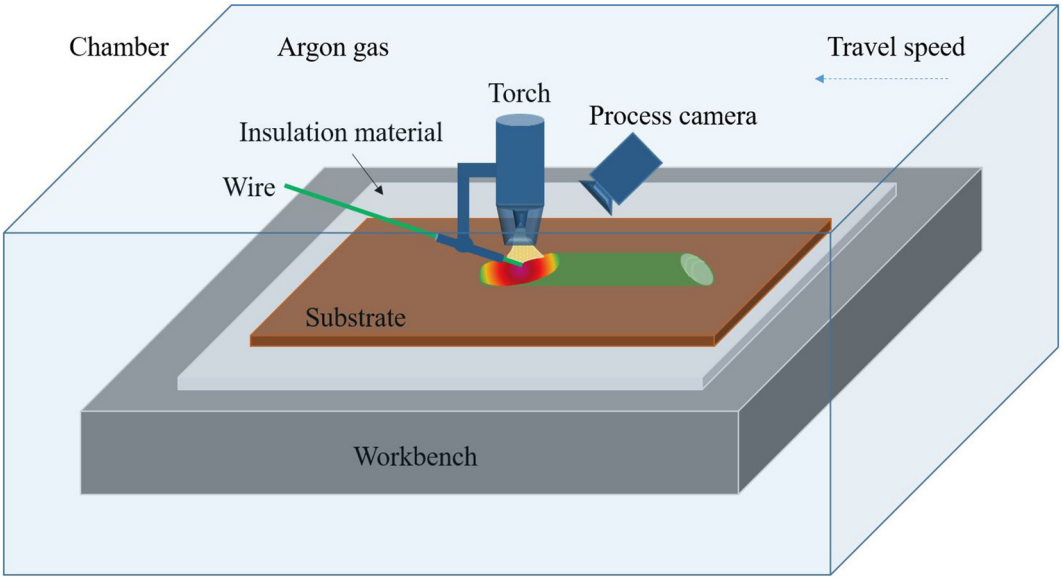

Fig. 1. Schematic of the experimental setup for the WPAAM process.

Table 1
Chemical composition (in wt%) of the Ti-6Al-4V substrate and wire.

	Al	V	Fe	C	N	H	O	Ti
Wire	6.08	3.80	0.122	0.019	0.008	0.001	0.15	Balance
Substrate	6.39	4.20	0.17	0.01	0.01	0.006	0.16	Balance

Table 2
Process parameters used in this study.

Parameter	Value (unit)	Parameter	Value (unit)
Arc current	200 A	WFS	0–5 m/min
Arc voltage	23.4 V	Wire diameter	1.2 mm
Travel speed	4.5 mm/s	Ambient temperature	300 K

means the cells are full of argon gas; $0 < \alpha < 1$ means the cells are in the transition region. Hence free surfaces can be captured by solving the transport equation of volume fraction [34]:

$$\frac{\partial \alpha}{\partial t} + \nabla \bullet (\alpha \mathbf{u}) = 0 \tag{4}$$

The normal vectors and the curvatures of the free surfaces can be described by solving the following equations:

$$\boldsymbol{n} = \frac{\nabla \alpha}{|\nabla \alpha|} \tag{5}$$

$$\kappa = -(\nabla \bullet \boldsymbol{n}) \tag{6}$$

The liquid-solid interface (mushy zone) changes during the WPAAM process. The enthalpy-porosity technique [35] was applied to implicitly track the time-dependent liquid-solid interface with a liquid fraction. The mushy zone was considered as a porous medium, with a linear relationship between the liquid fraction and temperature:

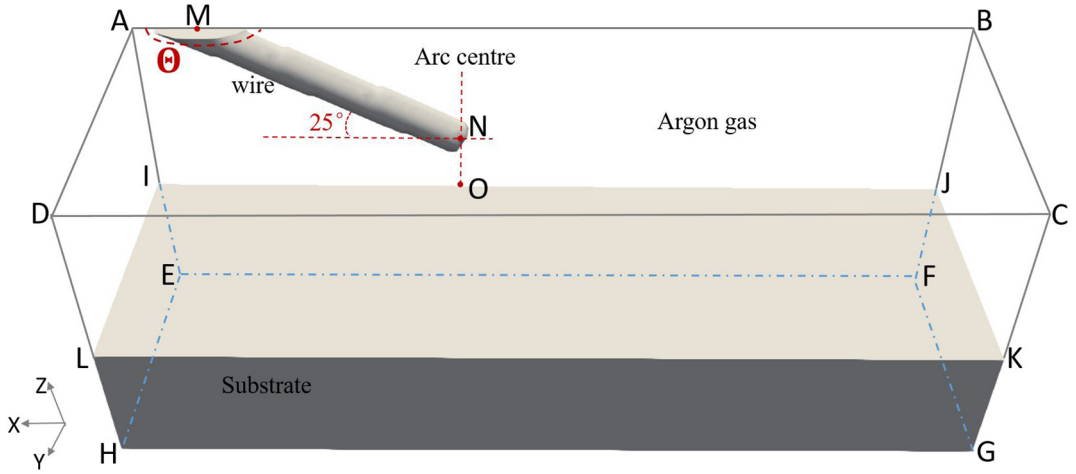

Fig. 2. Schematic of the geometry model in simulations.

Table 3
Nomenclature.

Symbol	Meaning and unit	Symbol	Meaning and unit
A_{mush}	mushy zone constant, kg m^{-3} s^{-1}	R_{a2}	rear radius in length of heat source, m
$a_1 - a_7$	coefficients used in arc shear stress mode	R_b	radius in width of heat source, m
C_p	specific heat, J kg^{-1} K^{-1}	T	temperature, K
C_{pg}	specific heat of gas, J kg^{-1} K^{-1}	T_l	liquidus temperature of metal, K
C_{pl}	specific heat of liquid, J kg^{-1} K^{-1}	T_s	solidus temperature of metal, K
$\mathbf{F}_g$	momentum source of gravity, N m^{-3}	T_{amb}	ambient temperature, K
$\mathbf{F}_m$	momentum source of Darcy force vector, N m^{-3}	T_{ref}	reference temperature, K
$\mathbf{F}_s$	momentum source of surface force vector, N m^{-3}	t	time, s
$\mathbf{F}_v$	momentum source of body force vector, N m^{-3}	U	arc voltage, V
$\mathbf{F}_{em}$	momentum source of electromagnetic force, N m^{-3}	$\mathbf{u}$	velocity vector, m/s
$\mathbf{F}_{as}$	momentum source of arc shear stress, N m^{-3}	$\boldsymbol{u_b}$	boundary velocity vector, m/s
$\mathbf{F}_{ap}$	momentum source of arc pressure, N m^{-3}	$\mathbf{u_t}$	velocity vector of travel speed, m/s
$\mathbf{F}_{ms}$	momentum source of Marangoni force, N m^{-3}	$\mathbf{u_w}$	velocity vector of wire-feeding speed, m/s
$\mathbf{F}_{st}$	momentum source of surface tension, N m^{-3}	v_t	travel speed, m/s
F_{emx}	x component of electromagnetic force, N m^{-3}	x	x-coordinate value, m
F_{emy}	y component of electromagnetic force, N m^{-3}	x_0	x-coordinate value of starting location, m
F_{emz}	z component of electromagnetic force, N m^{-3}	y	y-coordinate value, m
$\mathbf{g}$	acceleration of gravity, m s^{-2}	y_0	y-coordinate value of starting location, m
g_{as}	distribution function of arc shear stress	z	z-coordinate value, m
h	enthalpy, J kg^{-1}	z_0	z-coordinate value of starting location, m
h_c	heat convection coefficient, W m^{-2} K^{-1}	α	volume fraction function of fluid
h_{ref}	reference enthalpy, J kg^{-1}	β	liquid fraction
I	arc current, A	β_T	thermal expansion coefficient, K^{-1}
k	thermal conductivity, W m^{-1} K^{-1}	κ	curvature of free surface, m^{-1}
k_b	Stefan-Boltzmann constant, W m^{-2} K^{-4}	ε_0	a small constant avoid the division by zero.
L_0	thickness of base plate, m	ε_r	radiation emissivity
L_m	latent heat of melting, J kg^{-1}	η	arc heat efficiency
$\boldsymbol{n}$	normal vector to the local free surface, m	π	circumference ratio
p	pressure, Pa	δ_s	a delta function, m^{-1}
p_{max}	maximum arc pressure, Pa	$\rho\ \rho_g\ \rho_l$	density, density of gas and liquid, kg m^{-3}
q_{en}	energy distribution of plasma arc, W m^{-2}	σ	surface tension (ST) coefficient, N m^{-1}
q_{heat}	arc heat source, W m^{-3}	σ_j	distribution of arc current density, m
q_{loss}	heat loss due to radiation and convection, W m^{-3}	σ_p	distribution of arc pressure density, m
r	radius value of XY plane, m	$\frac{d\sigma}{dT}$	ST temperature coefficient, N m^{-1} K^{-1}
r_d	Parameter used in arc shear stress model, m	$\boldsymbol{\tau}_{as}$	vector of arc shear stress, Pa
$\boldsymbol{r}$	radius vector of XY plane, m	$\vec{\tau}_s$	unit vector of arc shear stress
R	radius of Gaussian arc heat source	τ_{max}	maximum arc shear stress, Pa
R_{a1}	front radius in length of heat source, m	$\mu;\ \mu_m$	viscosity, Pa s; permeability, H m^{-1}

$$\beta = \begin{cases} 0 & T \le T_s \\ \dfrac{T - T_s}{T_l - T_s} & T_l > T > T_s \\ 1 & T \ge T_l \end{cases} \tag{7}$$

Since the mushy zone was treated as a porous medium, the liquid fraction equal to the porosity can act as a blocker to reduce the flow in this region and eliminate the velocity in the solid region where the liquid fraction is 0. The Darcy force due to the reduced porosity in the mushy zone is as follows:

$$\mathbf{F}_m = \frac{(1-\beta)^2}{\beta^3 + \varepsilon_0} A_{mush}(\mathbf{u} - \mathbf{u}_t - \mathbf{u}_w) \tag{8}$$

where ε_0 was set as 0.001. The A_{mush} was set to 2×10^6 considering the fast velocity drop and convergent computation [30]. The energy change caused by the phase transformation is as follows:

$$h = h_{ref} + \int_{T_{ref}}^{T} C_p dT + \beta L_m \tag{9}$$

2.2.3. Arc surface heat source model

In this study, an arc surface heat source model was developed, which considers the arc energy shading effect from the filler wire and a deformed free surface. Fig. 3 shows the schematic of the development of the arc surface heat source model. First, as shown in Fig. 3(a), the arc energy flux needs to be described. In the arc surface heat source model, the arc dynamics was not calculated directly but treated as heat and force sources to make the computation faster, following work developed in previous models [24–27,29,36]. A Gaussian distribution was assumed for the current density and arc energy flux incident on the filler wire, defined by previous theoretical and experimental measurements [36,37]:

$$q_{en} = \eta \bullet \frac{3UI}{\pi R^2} \bullet exp\left(-\frac{3r^2}{R^2}\right) \tag{10}$$

where the energy absorption efficiency η and the radius of the arc energy distribution R are only related to the equipment and materials used. In this study we used 0.56 and 6 mm, respectively, according to the experimental measurement from reference [37]; the heat source radius of XY plane, $r = \sqrt{(x - x_0 - v_t t)^2 + (y - y_0)^2}$. From the process images [Fig. 10], the arc length in the travel speed direction seemed enlarged on the substrate because of the effect of wire and deposit on the arc, compared with the Gaussian distribution described in Eq. (10). To get an accurate melt pool length in the simulation compared with the experiments, the length R_b of the arc energy distribution in the rear melt pool was increased. Thus, arc energy flux incident on the substrate can be described as a double ellipsoid surface distribution as shown in the following equation [38]:

$$q_{en} = \begin{cases} \eta \bullet \dfrac{6UI}{(R + R_b)R\pi} \bullet exp\left(-\dfrac{3r^2}{R^2}\right) & (r_1 > 0) \\ \eta \bullet \dfrac{6UI}{(R + R_b)R\pi} \bullet exp\left(-\dfrac{3r_1^2}{R_b^2} - \dfrac{3r_2^2}{R^2}\right) & (r_1 \le 0) \end{cases} \tag{11}$$

where $r_1 = x - x_0 - v_t t$, $r_2 = y - y_0$, the radius of the major axis of the back ellipse (enlarged arc length) R_b was 9 mm used in the study.

Then, the irradiated regions by the arc energy need to be defined. Fig. 3(b) shows the irradiated regions in yellow colour, and underneath the wire there is no irradiation on the surface of the substrate or melt pool (green colour) due to the shading effect. In the whole calculation domain, we first located the dynamic free surface using the VOF value ($0.05 \le \alpha \le 0.95$). Then, we scanned the whole domain and used a parameter $\varphi_z(x,y)$ to define the top free surface (irradiated regions) in the z-axis direction. We further employed a Delta function $\delta_s = |\nabla \alpha|$

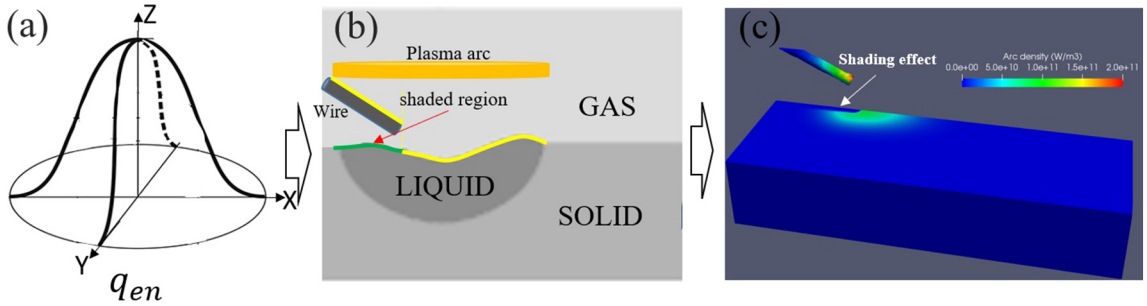

Fig. 3. Schematic of the development of the arc surface heat source model: (a) arc energy flux; (b) incidence of the heat flux on the top free surface, including the wire and unshaded melt pool and substrate; (c) shading effect in all dimensions.

[39] to transform arc energy flux q_{en} into the defined top free surface. So, only the top free surface defined by $\varphi_z(x,y)$ was irradiated by arc energy. Considering that the plasma arc is mainly absorbed in the metal region rather than the gas region of the free surface, we redistributed the arc energy toward the metal region with a higher ρC_p for the factor $\frac{2\rho C_p}{(\rho_l C_{pl}+\rho_g C_{pg})}$ [40]. Hence, the arc surface heat source is described as follows:

$$q_{heat} = q_{en}\varphi_z(x,y)\delta_s\frac{2\rho C_p}{\left(\rho_l C_{pl}+\rho_g C_{pg}\right)} \tag{12}$$

User define functions (UDF) was used to deal with the arc energy source term [Eq. (12)]. The total arc energy input in the whole calculation domain was calculated and kept as a constant. The arc energy heat source incident on the wire and substrate (including the melt pool) was developed, and the arc energy shading effect in all dimensions was considered, as shown in Fig. 3(c).

2.2.4. Driving forces

Two types of driving forces work on the fluids in the WPAAM process. One of them is the body force impacting on the volume of fluids, including gravity and buoyancy, and electromagnetic forces:

$$\mathbf{F}_v = \mathbf{F}_g + \mathbf{F}_{em} \tag{13}$$

The temperature difference produces a density difference, which results in the buoyancy force in the direction of the gravity vector. Boussinesq approximation was used to consider the density changes with the temperature. Gravity and buoyancy force can be expressed as:

$$\mathbf{F}_g = \rho\mathbf{g} - \rho\beta(T - T_{ref})\mathbf{g} \tag{14}$$

The electromagnetic forces in three different directions were introduced into the model using the simplified equations proposed by K. Tsao and C. Wu [36]:

$$F_{emx} = -\frac{\mu_m I^2}{4\pi^2\sigma_j^2 r}exp\left(-\frac{r^2}{2\sigma_j^2}\right)\left[1-exp\left(-\frac{r^2}{2\sigma_j^2}\right)\right]\left(1-\frac{z}{L_0}\right)^2\frac{(x-x_0-v_t t)}{r} \tag{15}$$

$$F_{emy} = -\frac{\mu_m I^2}{4\pi^2\sigma_j^2 r}exp\left(-\frac{r^2}{2\sigma_j^2}\right)\left[1-exp\left(-\frac{r^2}{2\sigma_j^2}\right)\right]\left(1-\frac{z}{L_0}\right)^2\frac{(y-y_0)}{r} \tag{16}$$

$$F_{emz} = -\frac{\mu_m I^2}{4\pi^2\sigma_j^2 r}exp\left(-\frac{r^2}{2\sigma_j^2}\right)\left(1-\frac{z-z_0}{L_0}\right) \tag{17}$$

The other type of driving forces is the surface force impacting on the free surface, including surface tension, Marangoni shear stress, arc pressure, and arc shear stress. These surface forces mainly control the surface flow and the deformation of the time-varying free surface. Recoil pressure was not considered in this model as the evaporation in the WPAAM process is considered insignificant [30].

$$\mathbf{F}_s = \mathbf{F}_{st} + \mathbf{F}_{ms} + \mathbf{F}_{ap} + \mathbf{F}_{as} \tag{18}$$

The surface tension pressure is normal to the free surface:

$$\mathbf{F}'_{st} = \sigma\kappa\boldsymbol{n} \tag{19}$$

The Marangoni effect is the mass transfer and an interface between two fluids due to a surface tension gradient caused by a concentration gradient or a temperature gradient. In high-energy metal welding or AM, the temperature gradient is generally considered the primary factor leading to Marangoni shear stress. Therefore, the Marangoni shear stress can be expressed as:

$$\mathbf{F}'_{ms} = \nabla_s\sigma = \frac{d\sigma}{dT}(\nabla T - \boldsymbol{n}(\boldsymbol{n}\bullet\nabla T)) \tag{20}$$

where ∇_s represents the surface gradient operator.

In the simulation of arc welding processes and AM processes, arc pressure is usually regarded as a Gaussian distribution [30]. In this study, the arc pressure was defined as follows:

$$\mathbf{F}'_{ap} = p_{max}exp\left(-\frac{r^2}{2\sigma_p^2}\right)\boldsymbol{n} \tag{21}$$

where p_{max} was set to 1853 Pa, which was measured by using the small-hole method with an arc current of 200 A [30]; σ_p used in this study was 0.78 mm [30].

Arc shear stress is generated by the friction between the arc flow and the moving surface of the melt pool. It is dependent on the dynamic viscosity and radial velocity of the arc. In this model, the arc shear stress was considered to have an empirical axisymmetric distribution [30]:

$$\boldsymbol{\tau}_{as} = \tau_{max}g_{as}(r)\widetilde{\boldsymbol{\tau}}_s \tag{22}$$

$$g_{as}(r) = \begin{cases} a_1 r^3 + a_2 r^2 + a_3 r + a_4 \; r \le r_d \\ a_5 exp\left(-\frac{r}{a_6}\right) + a_7 \; r > r_d \end{cases} \tag{23}$$

$$\widetilde{\boldsymbol{\tau}}_s = \frac{\boldsymbol{r} - \boldsymbol{n}(\boldsymbol{rn})}{|\boldsymbol{r} - \boldsymbol{n}(\boldsymbol{rn})|} \tag{24}$$

where $\boldsymbol{r} = (x - x_0 - v_t t, y - y_0, z_0)/|(x - x_0 - v_t t, y - y_0, z_0)|$. We adopted the value of the constant coefficients $a_1 - a_7$ and r_d in reference [41] in our simulations. Besides, in this study, τ_{max} was set to 100 N/m^2 [30,41].

Based on the continuum surface force (CSF) method [39], surface forces were imposed as volume forces in the free surface cells through the Delta function δ_s. To consider the arc pressure shading effect, like the arc energy, the arc force only applied on the top free surface by using the defining parameter $\varphi_z(x,y)$. The volume forces in the free surface cells could generate a high shear rate in the gas phase due to the very low density compared with the metal phase, which can cause a high velocity in the gas phase. To prevent the gas phase velocity from being too high, a multiplier term $\frac{2\rho}{(\rho_l+\rho_g)}$ was used for the volume forces [39]. Therefore,

the surface forces are expressed as follows:

$$\mathbf{F}_{st} = \mathbf{F}'_{st}\delta_s\frac{2\rho}{(\rho_l+\rho_g)} \tag{25}$$

$$\mathbf{F}_{ms} = \mathbf{F}'_{ms}\delta_s\frac{2\rho}{(\rho_l+\rho_g)} \tag{26}$$

$$\mathbf{F}_{ap} = \mathbf{F}'_{ap}\varphi_z(x,y)\delta_s\frac{2\rho}{(\rho_l+\rho_g)} \tag{27}$$

$$\mathbf{F}_{as} = \boldsymbol{\tau}_{as}\varphi_z(x,y)\delta_s\frac{2\rho}{(\rho_l+\rho_g)} \tag{28}$$

2.2.5. Boundary conditions

Table 4 illustrates the boundary conditions employed in this study. On the external boundaries, the heat loss caused by gas convection and thermal radiation was considered:

$$k\frac{\partial T}{\partial \boldsymbol{n}} = -h_c(T-T_{amb}) - \varepsilon_r k_b\frac{T^4-T_{amb}^4}{T-T_{amb}} \tag{29}$$

On the free surface, the heat loss caused by convection and thermal radiation was considered, while the heat loss caused by evaporation was neglected. By performing the same treatment to the arc surface heat source, the heat loss fluxes on the free surface can be described as follows:

$$q_{loss} = -\left(h_c(T-T_{amb}) + \varepsilon_r k_b\frac{T^4-T_{amb}^4}{T-T_{amb}}\right)\delta_s\frac{2\rho C_p}{\left(\rho_l C_{pl}+\rho_g C_{pg}\right)} \tag{30}$$

2.2.6. Numerical implementation

This study used the commercial CFD solver Ansys-Fluent 2019R2 to solve the governing equations and VOF equation. The pressure-velocity coupling was solved by using the PISO algorithm. The Body Force Weighted scheme was adopted to discretise the pressure equation, while the second-order upwind scheme was adopted to discretise the momentum equation and the energy equation. The first-order implicit scheme was adopted to discretise the transient formulation. The explicit scheme and the geometric reconstruction scheme were used to solve the volume fraction formulation.

An asymmetric boundary was used in the width direction, as shown in Table 4. The range of the computation domain was $0 \le x \le 38$ mm, $0 \le y \le 12$ mm, and $-7 \le z \le 6$ mm. The substrate thickness used in the simulation was 7 mm, which is the same as in the experiment. The distance between the central tip of the wire at the arc centre and the top surface of the substrate was 3 mm. As shown in Fig. 4, non-uniform hexahedral meshes were used for the simulation domain. In the computation domain ($0 \le x \le 38$ mm, $0 \le y \le 7$ mm, and $-2 \le z \le 6$ mm) that is near the melted zone, a small mesh size of 0.2 mm was used to guarantee the accuracy of the simulation. A coarse mesh size of 1.0 mm was removed from the melted zone to decrease the mesh amount. A time step with a value between 2.5×10^{-5}–5×10^{-5} s was used to obtain a robust convergence. The thermophysical properties of Ti6Al4V alloy and other physical parameters used in the simulation are listed in Table 5.

Table 4
Boundary conditions (the geometry is shown in Fig. 2).

Boundary	Type	Momentum	Energy
ADLI, CDLK, BCKJ, FGKJ ABCD (without Θ)	Pressure outlet	Atmospheric pressure	$T = 300$ K (backflow)
Θ	Velocity inlet (metal phase)	$\boldsymbol{u_b} = \boldsymbol{u_w}$	$T = 300$ K
EFGH, GHKL	Wall	$\boldsymbol{u_b} = \mathbf{0}$	Eq. (29)
EHLI	Velocity inlet	$\boldsymbol{u_b} = \boldsymbol{u_t}$	$T = 300$ K
ABFE	Symmetry	$u_{by} = 0, \frac{\partial \boldsymbol{u_b}}{\partial \boldsymbol{n}} = \mathbf{0}$	$\frac{\partial T}{\partial \boldsymbol{n}} = 0$

3. Results and discussion

Fig. 5 shows the evolution of the metal transfer process of WPAAM Ti6Al4V with a WFS of 3 m/min. The metal transfer process can be better understood by viewing the submitted Movie 1. At the beginning of the deposition, the plasma arc started to heat the feeding wire and the plate. The wire approached to the arc centre quickly and the wire tip became melted [Fig. 5(a)]. It flowed downward under the arc force (pressure and shear stress) and gravity and grew as a droplet [Fig. 5(b)]. When the droplet touched the melt pool (or substrate), it was pulled into the melt pool by the strong surface tension of the liquid Metal, and a temporary liquid bridge was formed. The necking occurred at the liquid bridge [Fig. 5(c)], and then the liquid bridge soon broke because of the imbalance of the arc force, surface tension and gravity. As the process proceeded, the wire was continuously fed and heated by the plasma arc. The droplet at the wire tip grew again [Fig. 5(d)]. It then generated a new liquid bridge which broke with the unbalanced forces [Fig. 5(e)], and soon another new droplet grew [Fig. 5(f)]. This cycle repeated until the end of the process. Here in this paper, this type of metal transfer is called droplet-liquid bridge mode. Besides, the process behaviour of the wire melting, flowing down, and transferring at the WFS of 3 m/min was captured by a process camera, as shown in the submitted Movie 2. It can be seen that the simulated metal transfer process is in good agreement with the experimental data.

To study the evolution of the coupling behaviours of the fluid flow and metal transfer dynamics, the longitudinal central slice and the traverse slice are taken from the model, as shown in Fig. 6 and Fig. 7, respectively. The transverse slice was taken at 1.2 mm behind the arc centre. The flow behaviours can be better viewed from the submitted Movie 3 and Movie 4. At the beginning of the process, the filler wire was soon melted and driven by the arc force with a downward flow of about 0.32 m/s [Fig. 6(a)]. The temperature of the heated substrate was close to the melting point [Fig. 7(a)]. The continuously melted wire was soon blown down onto the hot substrate and then flowed backwards [Fig. 6(b)] and sideward [Fig. 7(b)]. As the process continued, a small melt pool was generated and flowed at a backward velocity of about 0.3 m/s [Fig. 6(c)] and a lateral velocity of about 0.24 m/s [Fig. 7(c)], driven by Marangoni shear stress and arc shear stress. As soon as a temporary liquid bridge was formed, an intensive downward flow with a high velocity of about 0.54 m/s occurred, driven by the surface tension of the melt pool and gravity [Fig. 6(c)]. The strong impact of the metal transfer on the melt pool accelerated the fluid flow. As a result, the backward and lateral flows were accelerated to a speed of approximately 0.45 m/s [Fig. 6(d)] and 0.32 m/s [Fig. 7(d)], respectively, increasing the length and the width of the melt pool.

As the process proceeded, the melt pool grew longer and wider, as shown in Fig. 6(e) and Fig. 7(e). When the high-velocity downward flow (about 0.6 m/s) hit the melt pool again, a counterclockwise vortex occurred at the front of the melt pool. The impact effect was transferred to the back and the side of the melt pool, causing backward and lateral waves. The velocity of the backward flow at the rear of the melt pool rose from 0.16 m/s [Fig. 6(e)] to 0.36 m/s [Fig. 6(f)], while the velocity of the lateral flow at the edge of the melt pool rose from 0.2 m/s [Fig. 7(e)] to 0.34 m/s [Fig. 7(f)]. This periodic flow pattern in the melt pool caused by metal transfer occurred throughout the whole deposition process, which may cause ripples, or even humping defects. Except for the metal transfer impact, the surface fluid flow in the melt pool is supposed to be mainly governed by the Marangoni shear stress and arc shear stress [30]. Since only a low plasma gas rate of 0.8 l/min was used in this study, the maximum arc shear stress was only 100 N/m^2, which is much smaller than the Marangoni shear stress (about 500 N/m^2). When the melt pool was in a quasi-steady state [Fig. 7(e) and (f)], its length

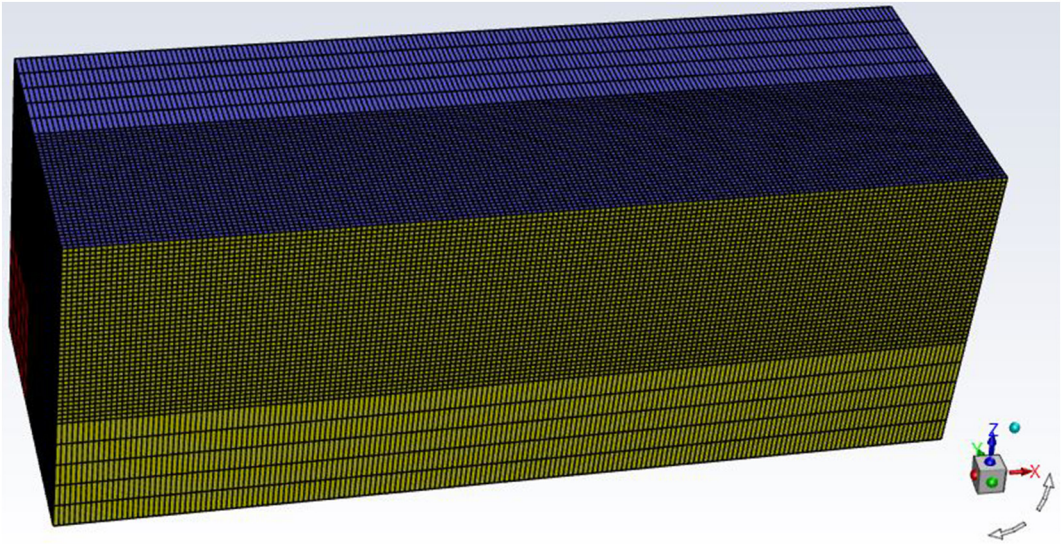

Fig. 4. Schematic sketch of the meshed geometry.

Table 5
Thermo-physical properties of Ti6Al4V alloys and other physical parameters.

Property (unit)	Value
Density (kg m^{-3})	4420 [42]
Specific heat (J kg^{-1} K^{-1})	Temperature-dependent [42]
Thermal conductivity (W m^{-1} K^{-1})	Temperature-dependent [42]
Solidus (K)	1878 [31,43]
Liquidus (K)	1928 [31,43]
Latent heat of melting (J kg^{-1})	2.85×10^5 [42]
Surface tension coefficient (N m^{-1})	1.33 [44]
Dynamic viscosity (N s m^{-2})	0.005 [43]
Thermal expansion coefficient (K^{-1})	8×10^{-6} [43]
Temperature coefficient of surface tension (N m^{-1} K^{-1})	-0.26×10^{-3} [44]
Convective heat transfer coefficient (W m^{-2} K^{-1})	80 [31]
Radiation emissivity	Temperature-dependent [42]
Atmospheric pressure (N m^{-2})	101,325
Stefan-Boltzmann constant (W m^{-2} K^{-4})	5.67×10^{-8}

was about 10.7 mm, which was consistent with the experimental data (about 11.4 mm) captured by the process camera.

As the process reached a quasi-steady state, the solidified bead cross-section also became stable. The values of the bead height, bead width and penetration depth were taken from the simulation [Fig. 8(a)] and were compared with the experimental measurements from the metallographic image [Fig. 8(b)]. It can be seen that the predicted bead shape matches reasonably well with the experimental data. The proposed model with detailed wire-feeding is reliable for investigating the complex heat and metal transfer, fluid flow behaviour, and bead shape formation of the WPAAM process.

Based on the wire-feeding model, the metal transfer behaviours of different WFS in the range of 1–5 m/min were further simulated and analysed, as shown in Fig. 9. With the increase of WFS, the location and the mode of metal transfer changed significantly. When the WFS was 1 m/min, the wire was melted at the edge of the arc. As the wire was melted continuously, a large droplet grew up at the tip of the wire [Fig. 9 (a)]. When the droplet was big (heavy) enough to overcome the surface tension, it fell into the melt pool. This type of metal transfer is usually called the globular-droplet mode. Since the metal transfer position is far from the arc centre, gravity dominates the metal transfer process. As the WFS increased, the wire melting position moved closer to the arc centre [Fig. 9(b)]. When the WFS increased to 3 m/min, the wire melting position reached the arc centre [Fig. 9(c)], and the droplet-liquid bridge mode as described earlier [Fig. 5] was formed. Assuming that the droplet formed at the arc centre is a ball with a diameter of 1.2 mm, the volume V_b and the effective area S_b under the arc pressure are 9.05×10^{-10} m^3 and 1.13×10^{-6} m^2, respectively. According to the formula of arc pressure [Eq. (21)], the average value within 0.6 mm of the arc centre $\mathbf{F}_{ap}'$ is about 1432 Pa. The gravity (force, $\rho V_b \mathbf{g}$) and the arc pressure (force, S_b) on the small droplet are 3.92×10^{-5} N and 1.62×10^{-3} N, respectively. The arc pressure on the small droplet is nearly two orders of magnitude greater than gravity. Thus, the arc pressure dominated the metal transfer before the melted wire touched the melt pool. In addition, it can be inferred from the arc pressure distribution that, compared with the arc pressure, the closer to the arc centre, the smaller the influence of gravity on the metal transfer process.

When the WFS increased to 4 m/min, the wire passed through the arc centre [Fig. 9(d)]. The melted wire first formed as a small droplet and then immediately pulled down when it contacted the melt pool, still following the droplet-liquid bridge mode. When the WFS increased to 5 m/min, the wire was only partially melted [Fig. 9(e)] before it entered the melt pool. The melted part of the wire was pulled down into the melt pool by surface tension. This type of metal transfer is called solid-liquid bridge mode. In this mode, surface tension and wire-feeding force dominate the metal transfer process. Fig. 10 shows the metal transfer images with the WFS of 1–5 m/min, captured by the process camera. By comparing the shape, position, and mode of the metal transfer, it can be concluded that the simulations are consistent with the experimental results. It further demonstrates that the wire-feeding model can reproduce the metal transfer dynamics with different WFS.

Fig. 11 shows the surface bead profile with the WFS of 0–5 m/min after the deposition process. While the bead surface without wire feeding is very smooth [Fig. 11(a)], those with wire feeding are not, which demonstrates that the metal transfer impact has a significant effect on the melt pool flow patterns. The study of fluid flow behaviours coupled with the metal transfer dynamics is shown in Fig. 12. The longitudinal central slices and the transverse slices 1.2 mm behind the arc centre are presented after the deposition achieved a quasi-steady state. At a WFS of 1 m/min, the big droplet grew up gradually at the wire tip at the edge of the arc and was driven down by gravity to the melt pool at a relatively big distance from the wire tip. As a result, the period of the globular-droplet transfer was long, with a value of about 0.5 s or more. Large droplets hit the front part of the melt pool during the metal transfer, causing intensive waves to propagate to the back and side of the

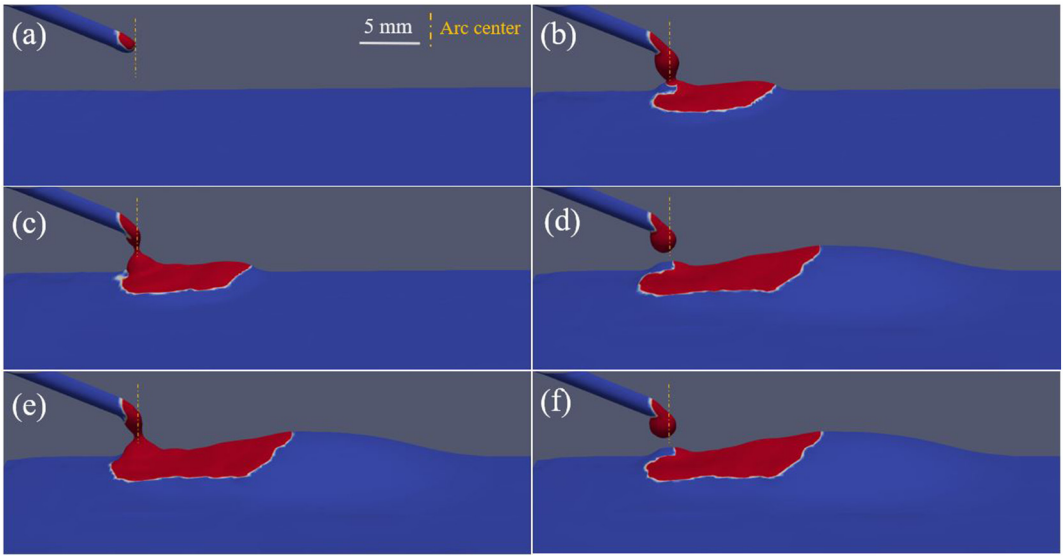

Fig. 5. Evolution of metal transfer process at the WFS of 3 m/min, the red colour part represents the melted metal: (a) 0.0706 s; (b) 0.5506 s; (c) 0.6226 s; (d) 3.2386 s; (e) 3.2626 s; (f) 3. 2866 s. (For interpretation of the references to colour in this figure legend, the reader is referred to the web version of this article.)

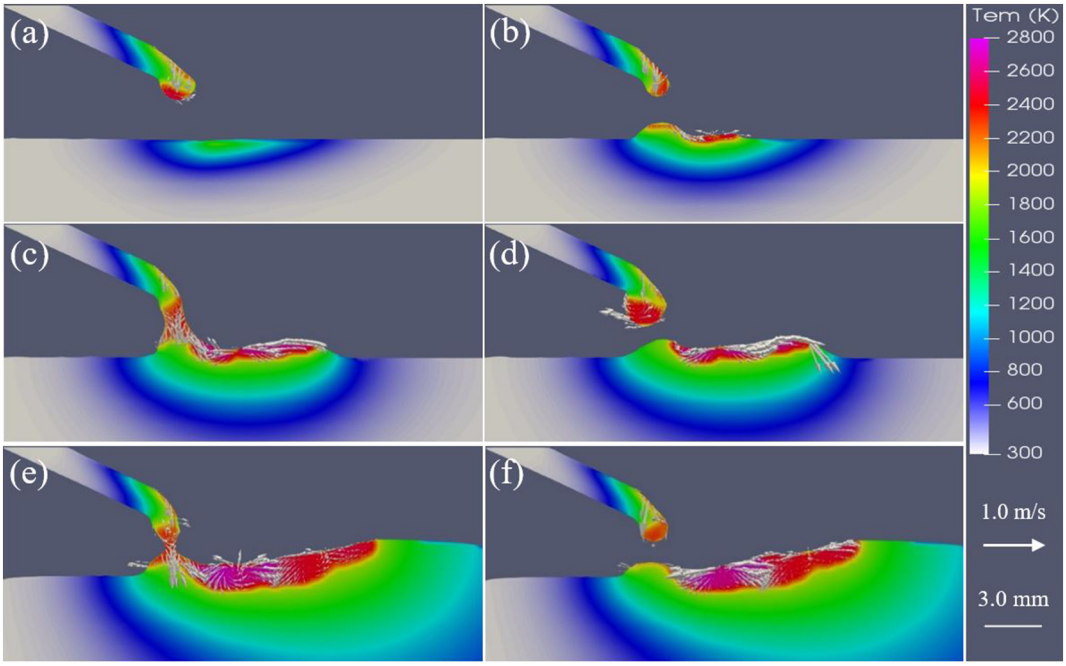

Fig. 6. Evolution of fluid flow in melt pool coupled the metal transfer dynamics with the WFS of 3 m/min at a longitudinal central slice: (a) 0.1186 s; (b) 0.2146 s; (c) 0.5746 s; (d) 0.6706 s; (e) 3.3106 s; (f) 3.3826 s.

melt pool. The backward flow velocity at the rear part of the melt pool soon increased from 0.15 m/s to approximately 0.56 m/s [Fig. 12(a)]. This sudden acceleration of the backward flow promoted more accumulation of the low-temperature melted Metal at the end of the melt pool and solidified there. Due to the long metal transfer cycle, there was no longer a continuous flow of melted Metal. Therefore, the periodic flow caused by the globular-droplet transfer usually results in large ripples and even humping defects [Fig. 10(a)]. As the WFS increased to 2 m/min or larger, the metal transfer changed to a smaller droplet or liquid bridge. For the droplet-liquid bridge transfer with the WFS of 3 m/min, the period of the small droplet formation and transfer driven by much larger forces (the arc pressure or surface tension of the melt pool) was significantly shorter compared with that at the globular-droplet transfer. It was only about 0.05 s. The period of the solid-liquid bridge transfer with the WFS of 5 m/min was also very short since the small droplet on the top surface of the wire grew up and was pulled by the melt pool quickly. It was about 0.048 s or less. As a result, the rear melt pool has a significantly smaller velocity difference with the value of about 0.21 m/s at the droplet-liquid bridge transfer (Fig. 6) and 0.18 m/s at the solid-liquid bridge transfer was obtained, compared with the value of about 0.41 m/s at the globular-droplet transfer. Those also illustrated that melt pool flow with the effect of a relatively high-frequency metal transfer was more stable. Therefore, when the WFS was 2–5 m/min [Fig. 12(c), (e), and (g)], the periodic flow caused by metal transfer was more stable and uniform than those with a WFS of 1 m/min, and only small ripples appeared on the surface of the bead [Fig. 11].

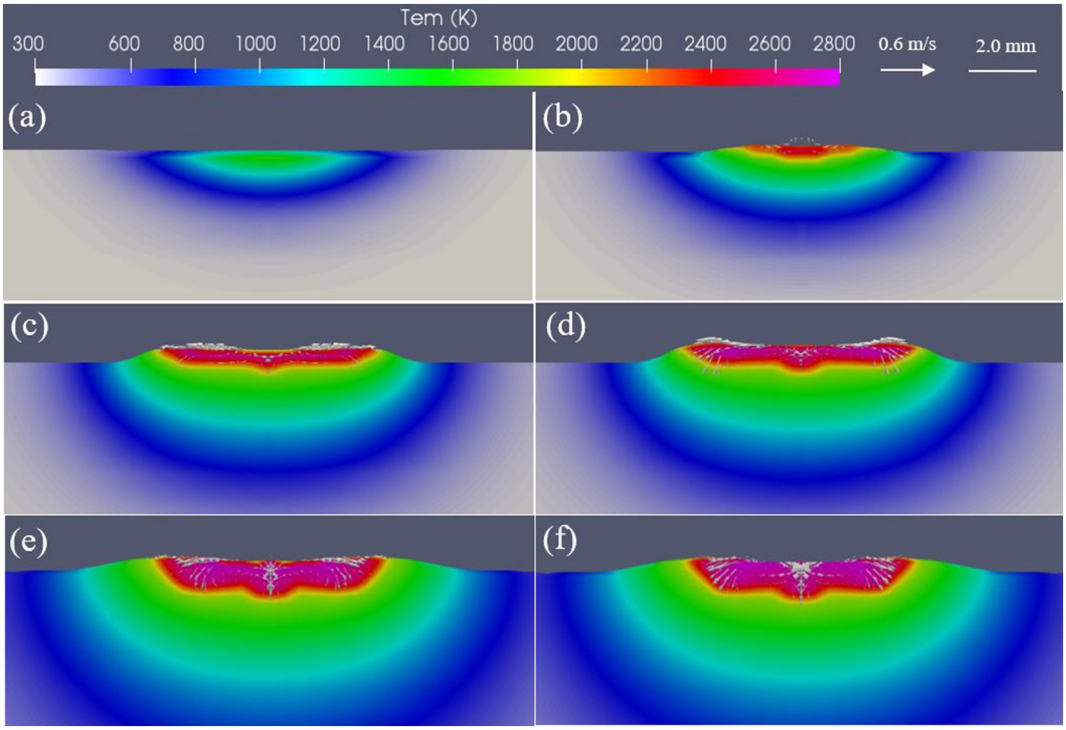

Fig. 7. Evolution of fluid flow in melt pool coupled the metal transfer dynamics with the WFS of 3 m/min at a transverse slice with 1.2 mm behind the arc centre: (a) 0.1186 s; (b) 0.2146 s; (c) 0.5746 s; (d) 0.6706 s; (e) 3.3106 s; (f) 3.3826 s.

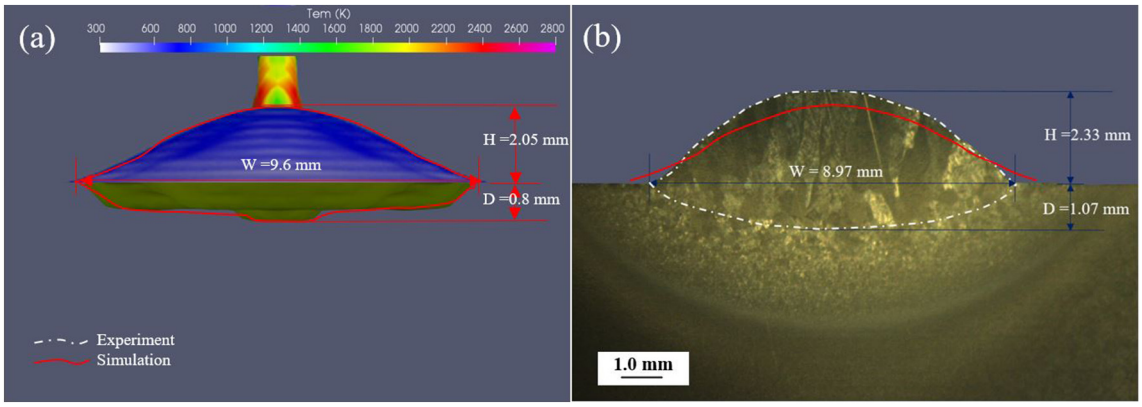

Fig. 8. Comparison of bead shape between (a) simulation and (b) experiment with the WFS of 3 m/min.

With the increase of WFS, the behaviour of the lateral flow changed significantly [Fig. 12(b), (d), (f), and (h)], and when the WFS was 1 m/min, a depression occurred due to the strong arc pressure acting on the surface of the melt pool. The maximum temperature at the centre of the melt pool was about 2860 K. The lateral flow velocity, mainly driven by Marangoni shear stress and metal transfer impact, reached about 0.46 m/s [Fig. 12(b)]. As the WFS increased to 2 and 3 m/min, the depression decreased gradually due to the arc shading effects from the wire, which reduced the arc pressure to the melt pool. The maximum temperature at the centre of the melt pool was about 2850 K and 2820 K, respectively. The velocities of the lateral flow of these two cases were 0.36 m/s and 0.34 m/s, respectively. When the WFS increased to 4 and 5 m/min, the melt pool became convex due to the strong arc shading effects and a large amount of metal transfer [Fig. 12(f) and (h)]. In addition, the maximum temperature at the centre of the melt pool dropped significantly to about 2730 K and 2680 K, respectively. It should be noted that at high WFS [Fig. 12(e), (g)], the cold wire was partially melted in the melt pool, which also contributed to the temperature drop of the melt pool. As a result, the lateral Marangoni flow decreased significantly due to the decrease in a temperature gradient. The velocities of the lateral flow dropped to 0.32 m/s and 0.25 m/s, respectively, for WFS of 4 m/min and 5 m/min.

Fig. 13 compares bead dimensions between experiments and simulations with the WFS of 2–5 m/min. Due to the humping defects, this comparison did not include the WFS of 1 m/min. The calculated bead dimensions, including the bead width, bead height, and penetration depth, are consistent with the experimental measurements. The bead height increased, and the penetration depth decreased as the WFS increased. The bead width first increased as the WFS increased from 2 m/min to 3.5 m/min and then decreased as the WFS increased to 5 m/min. The relative error of simulations compared with experiments is shown in Table 6. Generally, the errors are around or <10 %, which explicitly shows the good agreement between the simulated and experimental dimensions. It should be noted that the relatively significant errors of the bead height at the WFS of 5 m/min and the penetration depth at the WFS of 3 m/min. In a real experiment, the voltage

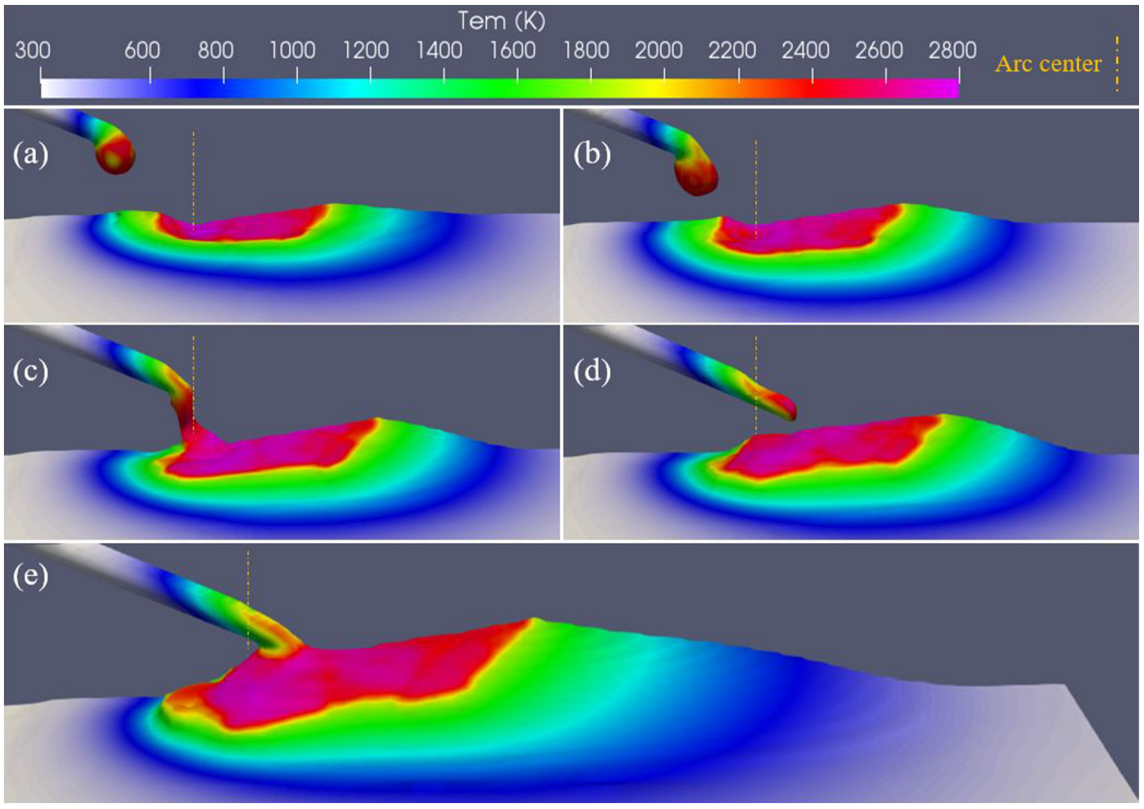

Fig. 9. Metal transfer behaviours with different WFS at 2.0 s: (a) 1 m/min; (b) 2 m/min; (c) 3 m/min; (d) 4 m/min; (e) 5 m/min.

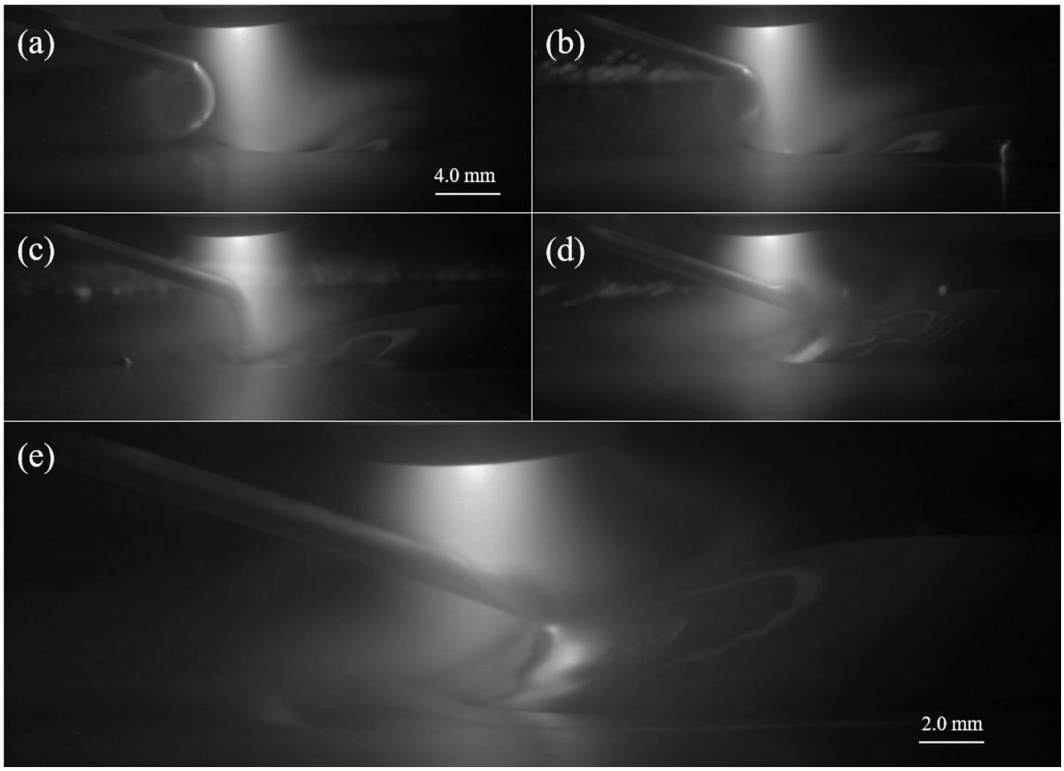

Fig. 10. Metal transfer images with different WFSs captured by a process camera: (a) 1 m/min; (b) 2 m/min; (c) 3 m/min; (d) 4 m/min; (e) 5 m/min.

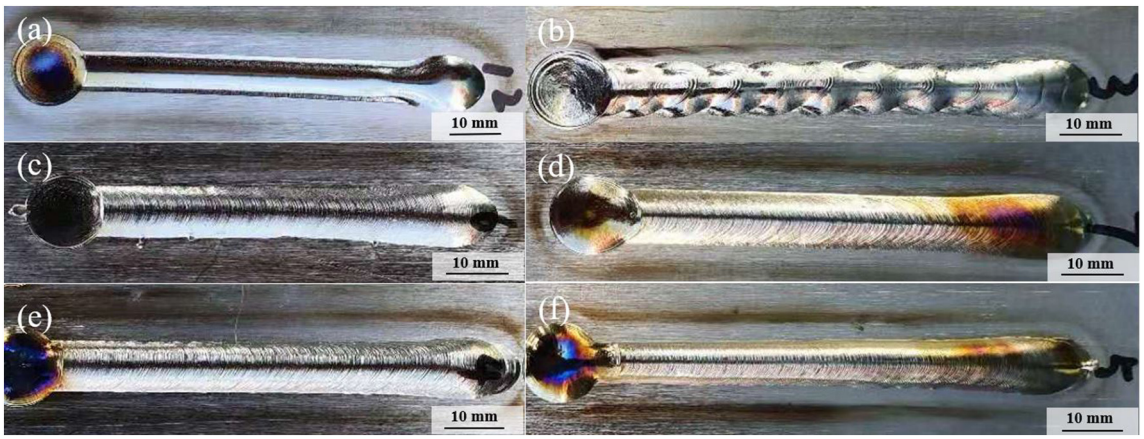

Fig. 11. Bead surface profiles with different WFS: (a) 0 m/min; (b) 1 m/min; (c) 2 m/min; (d) 3 m/min; (e) 4 m/min; (f) 5 m/min.

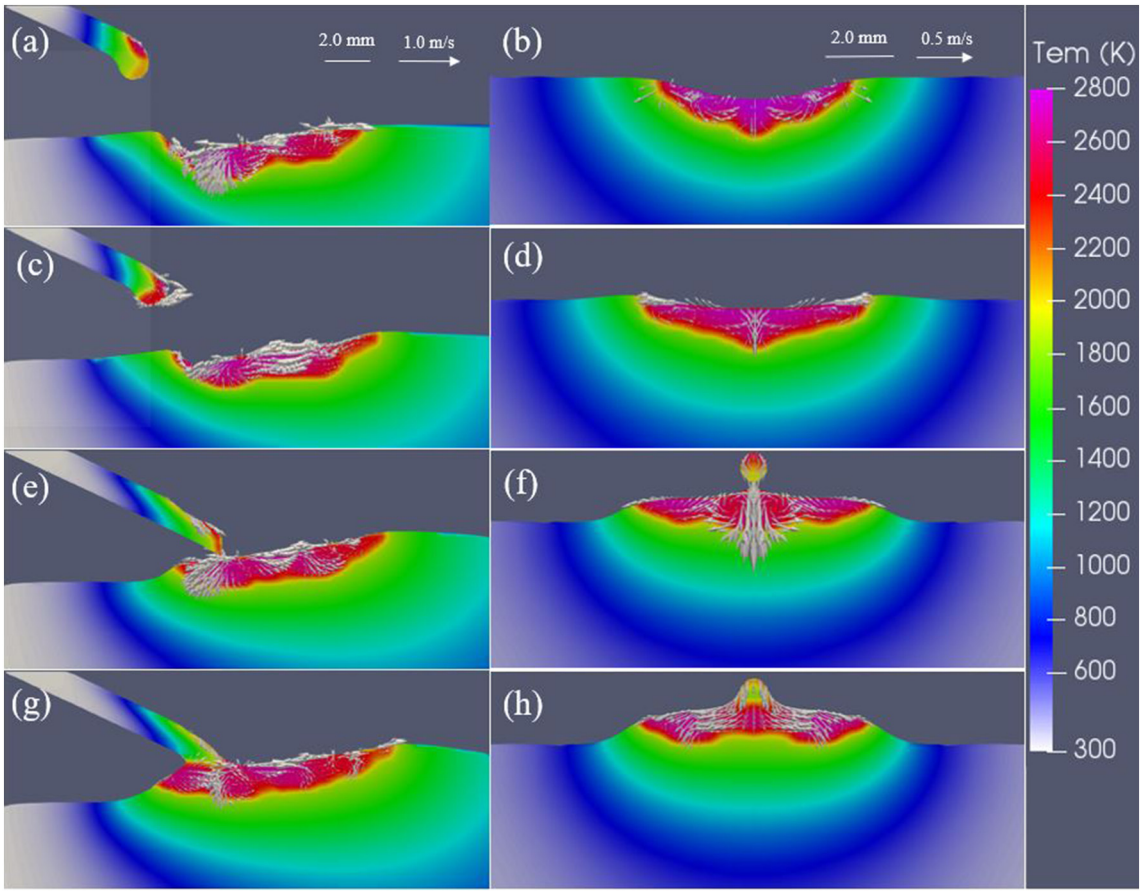

Fig. 12. Flow behaviours in a quasi-steady state (around 4 s) at the longitudinal central slice (the left figures) and transverse slice (1.2 mm behind the arc centre, the right figures) just after a metal transfer with different WFS: (a) and (b) 1 m/min; (c) and (d) 2 m/min; (e) and (f) 4 m/min; (g) and (h) 5 m/min.

decreased when the wire touched the melt pool [24,33], which caused the decrease of heat input at the WFS of 5 m/min. However, in the simulation, we used a constant heat input larger than that in the experiment, which caused the less bead height and wider bead width at the WFS of 5 m/min. Besides, the arc could flow around the wire [16] and produce an arc pressure on the melt pool under the wire, which was not considered in the model. At the WFS of 3 m/min, arc flows along the liquid bridge at the arc centre impacted the melt pool. That might produce an arc pressure on the melt pool. In the simulation, the arc pressure was shaded by the wire, which could cause a smaller penetration depth, especially at the WFS of 3 m/min.

To understand the bead width variation, the horizontal velocity (HV) of lateral flow with the WFS of 2–5 m/min was analysed, as shown in Fig. 14. As the WFS increased from 2 to 3 m/min, although the average temperature of metal transfer decreased from 2580 K to 2430 K, the maximum temperature at the melt pool centre only slightly decreased from 2850 K to 2820 K. The lateral Marangoni flow did not change too much. However, the depression of the melt pool significantly decreased from 0.22 mm to 0.1 mm due to the arc pressure shading effect. As a result, the HV of the lateral flow increased from 0.27 m/s to 0.33 m/s. As the WFS increased to 4 and 5 m/min, a relatively cold metal transfer (2150 K) or unmelt metal transfer (1900 K) occurred. In addition, the

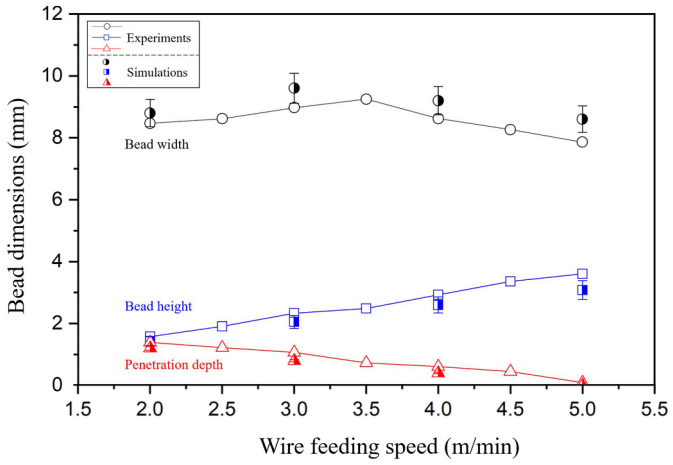

Fig. 13. Comparison of bead dimensions between simulations and experiments with the WFS of 2–5 m/min.

Table 6
Relative error of the simulated dimensions compared with the experimental data.

WFS	2 m/min	3 m/min	4 m/min	5 m/min
Error of bead width	3.9 %	7.0 %	7.1 %	9.4 %
Error of bead height	9.4 %	12.0 %	11.3 %	17.1 %
Error of penetration depth	13.7 %	25.2 %	18.0 %	10.0 %

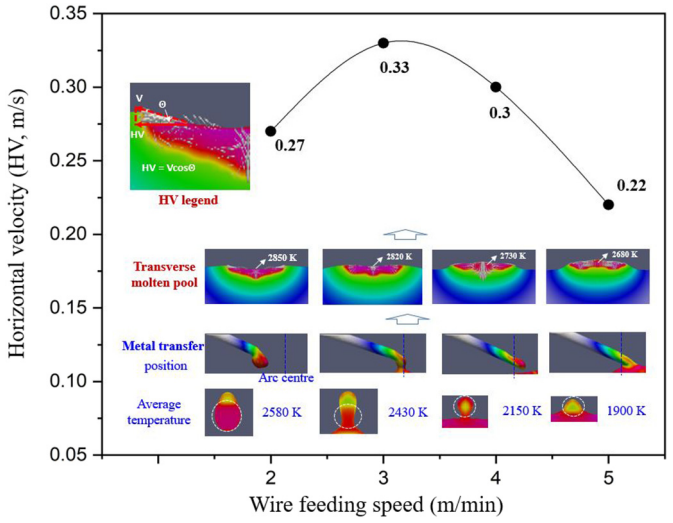

Fig. 14. Horizontal velocity variation of the lateral flow with the WFS of 2–5 m/min.

strong arc energy shading effect by the wire prevented the arc centre from heating the melt pool. Therefore, the maximum temperature at the metal pool centre dropped significantly to 2730 K and 2680 K, respectively, which caused the decrease of the lateral Marangoni flow. Meanwhile, the bead shape became convex. As a result, the HV of the lateral flow decreased to 0.3 m/s and 0.22 m/s, respectively, for the WFS of 4 m/s and 5 m/s, which explains the decrease of the bead width.

Since the previous models [26–31] did not consider the wire-feeding process, they were unable to include the arc pressure shading effect by the wire, resulting in excessive depression of the melt pool [30]. Furthermore, the arc energy shading effect, metal transfer temperature and impact, which can significantly affect the local temperature and fluid flow of the melt pool, were not incorporated into the melt pool dynamics either in the previous models.

The new model proposed here has been proven to be suitable for studying the complex coupling behaviour of metal transfer dynamics, flow patterns, and bead shape formation in the WPAAM process. The arc shading effects and metal transfer dynamics have been shown to significantly affect the depression, temperature, velocity and flow pattern of the melt pool and the final bead shape. The wire-feeding process, including metal transfer, should be included in the hydrodynamic WPAAM model as an essential element. This new model can be used as a theoretical tool and basis to better understand the underlying physical mechanisms and bead shape control in the WPAAM process.

4. Conclusions

A new 3D model with detailed wire-feeding simulation for the WPAAM process has been developed. The coupling behaviours of heat and metal transfer, fluid flow and solidified bead shape were investigated numerically. Good agreements of the metal transfer process, flow patterns, and bead shape have been obtained between simulations and experiments. More details are the following:

(1) With the detailed modelling of the wire melting and droplet transfer, this new model can be used to study the metal transfer behaviour, which is an important aspect of the WPAAM process. As the WFS increased from 1 m/min to 5 m/min, three metal transfer modes were observed, changing from the globular-droplet mode to the droplet-liquid bridge mode and then to the solid-liquid bridge mode, and this phenomenon was captured by the model accurately. From the numerical analysis, it can be concluded that gravity is the main driven force for the globular-droplet mode; the arc force and surface tension dominate the droplet-liquid bridge mode; the surface tension and wire-feeding force govern the solid-liquid bridge mode.

(2) As the WFS increased from 2 to 5 m/min, the bead width first increased and then decreased, which can be explained using the variation of the horizontal velocity of the lateral flow. The increase of the bead width was caused by the increase of the horizontal velocity, mainly due to the decrease of the melt pool depression from the arc pressure shading effect. The decrease of the bead width was caused by the reduction of the horizontal velocity of the lateral flow, mainly due to the weakened lateral Marangoni flow. The lower lateral Marangoni flow was caused by the lower temperature of the melt pool centre, which was caused by the combined effect of the strong arc energy shading effect and the cold wire (partially melted in the arc) transfer.

(3) The metal transfer impact was shown as a significant driving force of the melt pool, producing a periodic flow pattern of the melt pool, resulting in ripples or even humping defects. The arc shading effect by the filler wire was shown to influence the melt pool dynamics, such as the surface depression, temperature, and flow velocity. Therefore, considering the wire-feeding process essential to model the metal transfer dynamics and arc shading effect is necessary for a comprehensive hydrodynamic model of WPAAM.

Supplementary data to this article can be found online at https://doi.org/10.1016/j.jmapro.2022.09.012.

Declaration of competing interest

The authors declare that they have no known competing financial interests or personal relationships that could have appeared to influence the work reported in this paper.

Acknowledgements

The authors would like to thank the NEWAM project (EP/R027218/1) for financial support. The authors would like to thank Professor YuMing Zhang, Professor Anthony Bruce Murphy and the reviewers for their constructive comments and suggestions. The authors also would like to thank Nisar Shah, John Thrower, Guangyu Chen, and Steve Pope from Cranfield University for the experimental technical support and Xingwang Bai from the University of South China for valuable discussion of the model development.

References

[1] Williams S, Martina F, Addison A, Ding J, Pardal G, Colegrove P. Wire + Arc additive manufacturing. Mater Sci Technol 2016;32:641–7.
[2] Wu B, Pan Z, Ding D, Cuiuri D, Li H, Xu J, Norrish J. A review of the wire arc additive manufacturing of metals: properties, defects and quality improvement. J Manuf Process 2018;35:127–39.
[3] Zhang Y, Chen Y, Li P, Male AT. Weld deposition-based rapid prototyping: a preliminary study. J Mater Process Technol 2003;135:347–57.
[4] DebRoy T, Mukherjee T, Wei H, Elmer J, Milewski J. Metallurgy, mechanistic models and machine learning in metal printing. Nat Rev Mater 2020:1–21.
[5] Wu Y, Kovacevic R. Mechanically assisted droplet transfer process in gas metal arc welding. J Eng Manuf 2002;216:555–64.
[6] Ding J, Colegrove P, Mehnen J, Ganguly S, Sequeira Almeida PM, Wang F, Williams S. Thermo-mechanical analysis of wire and arc additive layer manufacturing process on large multilayer parts. Comput Mater Sci 2011;50:3315–22.
[7] Derekar K. A review of wire arc additive manufacturing and advances in wire arc additive manufacturing of aluminum. Mater Sci Technol 2018;34:895–916.
[8] Ya W, Hamilton K. On-demand spare parts for the marine industry with directed energy deposition: propeller use case. In: Int. Conf. Addit. Manuf. Prod. Appl. Cham: Springer; 2017. p. 70–81.
[9] Lin J, Lv Y, Liu Y, Xu B, Sun Z, Li Z, Wu Y. Microstructural evolution and mechanical properties of Ti-6Al-4V wall deposited by pulsed plasma arc additive manufacturing. Mater Des 2016;102:30–40.
[10] Wang C, Suder W, Ding J, Williams S. The effect of wire size on high deposition rate wire and plasma arc additive manufacture of Ti-6Al-4V. J Mater Process Technol 2021;288:116842.
[11] Zhang YM, Li P, Chen Y, Male AT. Automated system for welding-based rapid prototyping. Mechatronics 2002;12:37–53.
[12] Ouyang JH, Wang H, Kovacevic R. Rapid prototyping of 5356-aluminum alloy based on variable polarity gas tungsten arc welding: process control and microstructure. Mater Manuf Process 2002;17:103–24.
[13] Doumanidis H, Skordeli E. Optimising geometrical control of surface distributions in rapid prototyping deposition. Eur J Control 2000;6:279–89.
[14] Tanaka M, Terasaki H, Ushio M, Lowke J. A unified numerical modeling of stationary tungsten-inert-gas welding process. Metal Mater Trans A 2002;33:2043–52.
[15] Kumar A, DebRoy T. Toward a unified model to prevent humping defects in gas tungsten arc welding. Weld J 2006;85:292.
[16] Hu J, Tsai HL. Heat and mass transfer in gas metal arc welding, part II: the metal. Int J Heat Mass Transf 2007;50:808–20.
[17] Murphy AB, Chen FF, Xiang J, Wang HP, Thomas DG, Feng Y. Macrosegregation in the weld pool in metal inert-gas welding of aluminium. J Manuf Process 2021;61:111–27.
[18] Chen J, Schwenk C, Wu C, Rethmeier M. Predicting the influence of groove angle on heat transfer and fluid flow for new gas metal arc welding processes. Int J Heat Mass Transf 2012;55:102–11.
[19] Wu CS, Huo YS. Numerical analysis of keyhole geometry and temperature profiles in plasma arc welding. J Manuf Process 2013;15:593–9.
[20] Xu G, Cao Q, Hu Q, Zhang W, Liu P, Du B. Modelling of bead hump formation in high speed gas metal arc welding. Sci Technol Weld Join 2016;21(8):700–10.
[21] Lu F, Wang H, Murphy AB, Carlson B. Analysis of energy flow in gas metal arc welding processes through self-consistent three-dimensional process simulation. Int J Heat Mass Transf 2014;68:215–23.
[22] Wang X, Luo Y, Fan D. Investigation of heat transfer and fluid flow in high current GTA welding by a unified model. Int J Therm Sci 2019;142:20–9.
[23] Chen X, Mu Z, Hu R, Liang L, Murphy AB, Pang S. A unified model for coupling mesoscopic dynamics of keyhole, metal vapor, arc plasma, and weld pool in laser-arc hybrid welding. J Manuf Process 2019;41:119–34.
[24] Ríos S, Colegrove P, Williams S. Metal transfer modes in plasma Wire + Arc additive manufacture. J Mater Process Technol 2019;264:45–54.
[25] Hu R, Chen X, Yang G, Gong S, Pang S. Metal transfer in wire feeding-based electron beam 3D printing: modes, dynamics, and transition criterion. Int J Heat Mass Transf 2018;126:877–87.
[26] Ou W, Mukherjee T, Knapp GL, Wei Y, DebRoy T. Fusion zone geometries, cooling rates and solidification parameters during wire arc additive manufacturing. Int J Heat Mass Transf 2018;127:1084–94.
[27] Ou W, Wei Y, Liu R, Zhao W, Cai J. Determination of the control points for circle and triangle route in wire arc additive manufacturing (WAAM). J Manuf Process 2020;53:84–98.
[28] Hejripour F, Valentine DT, Aidun DK. Study of mass transport in cold wire deposition for wire arc additive manufacturing. Int J Heat Mass Transf 2018;125:471–84.
[29] Ogino Y, Asai S, Hirata Y. Numerical simulation of WAAM process by a GMAW weld pool model. Weld World 2018;62:393–401.
[30] Bai X, Colegrove P, Ding J, Zhou X, Diao C, Bridgeman P, Hönnige J, Zhang H, Williams S. Numerical analysis of heat transfer and fluid flow in multilayer deposition of PAW-based wire and arc additive manufacturing. Int J Heat Mass Transf 2018;124:504–16.
[31] Zhou X, Zhang H, Wang G, Bai X. Three-dimensional numerical simulation of arc and metal transport in arc welding based additive manufacturing. Int J Heat Mass Transf 2016;103:521–37.
[32] Cadiou S, Courtois M, Carin M, Berckmans W, LeMasson P. Heat transfer, fluid flow and electromagnetic model of droplets generation and molten pool behavior for wire arc additive manufacturing. Int J Heat Mass Transf 2020;148:119102.
[33] Cadiou S, Courtois M, Carin M, Berckmans W, Le masson P. 3D heat transfer, fluid flow and electromagnetic model for cold metal transfer wire arc additive manufacturing (Cmt-Waam). Addit Manuf 2020;36:101541.
[34] Hirt C, Nichols B. Volume of fluid (VOF) method for the dynamics of free boundaries. J Comput Phys 1981;39:201–25.
[35] Voller V, Brent A, Prakash C. The modelling of heat, mass and solute transport in solidification systems. Int J Heat Mass Transf 1989;32:1719–31.
[36] Tsao K, Wu C. Fluid flow and heat transfer in GMA weld pools. Weld J 1988;67:70s–5s.
[37] Chen G, Williams S, Ding J, Wang Y, Suder W. Split anode calorimetry for plasma arc energy density measurement with laser calibration. J Manuf Process 2022;78:71–81.
[38] Meng X, Qin G, Bai X, Zou Z. Numerical analysis of undercut defect mechanism in high speed gas tungsten arc welding. J Mater Process Technol 2016;236:225–34.
[39] Brackbill J, Kothe D, Zemach C. A continuum method for modeling surface tension. J Comput Phys 1992;100:335–54.
[40] Tang C, Tan J, Wong C. A numerical investigation on the physical mechanisms of single track defects in selective laser melting. Int J Heat Mass Transf 2018;126:957–68.
[41] Campbell S, Galloway A, McPherson N. Arc pressure and fluid flow during alternating shielding gases. Part 2: arc force determination. Sci Technol Weld Join 2013;18:597–602.
[42] Boivineau M, Cagran C, Doytier D, Eyraud V, Nadal M, Wilthan B, Pottlacher G. Thermophysical properties of solid and liquid Ti-6Al-4V (TA6V) alloy. Int J Thermophys 2006;27:507–29.
[43] Panwisawas C, Perumal B, Ward R, Turner N, Turner R, Brooks J, Basoalto H. Keyhole formation and thermal fluid flow-induced porosity during laser fusion welding in titanium alloys: experimental and modelling. Acta Mater 2017;126:251–63.
[44] Egry I, Holland-Moritz D, Novakovic R, Ricci E, Wunderlich R, Sobczak N. Thermophysical properties of liquid AlTi-based alloys. Int J Thermophys 2010;31:949–65.